

Three-dimensional hydrodynamic simulations of L_2 Puppis

Zhuo Chen^{1*} Jason Nordhaus^{2,3†} Adam Frank^{1‡} Eric G. Blackman^{1§} and Bruce Balick^{4¶}

¹Department of Physics and Astronomy, University of Rochester, Rochester NY, 14627

²Dept. of Science and Mathematics, National Technical Institute for the Deaf, Rochester Institute of Technology, Rochester, NY 14623

³Center for Computational Relativity and Gravitation, Rochester Institute of Technology, Rochester, NY 14623

⁴Department of Astronomy, University of Washington, Seattle, WA 98195, USA

in original form 2016 February 19

ABSTRACT

Recent observations of the L_2 Puppis system suggest that the Mira-like variable may be in the early stages of forming a bipolar planetary nebula (PN). As one of nearest and brightest AGB stars, and due to its status as a binary, L_2 Puppis serves as a benchmark object for studying the late-stages of stellar evolution. We perform global, three-dimensional, adaptive-mesh-refinement hydrodynamic simulations of the L_2 Puppis system with ASTROBEAR. The broad-band spectral-energy-distribution (SED) and synthetic observational images are post-processed from our simulations using the radiative transfer code RADMC-3D. Given the reported binary parameters, we are able to reproduce the current observational data if a short pulse of dense material is released from the AGB star with a velocity sufficient to escape the primary but not the binary. Such a situation could emanate from a thermal pulse, be induced by a periastron passage of the secondary, or could be launched if the primary ingests a planet.

Key words: ISM: structure — stars: winds, outflows — stars: AGB and post AGB — method: numerical

1 INTRODUCTION

Recent observations of the L_2 Puppis system suggest that the Asymptotic Giant Branch (AGB), Mira-like variable may be in the early stages of transitioning to a planetary nebula (PN) (Kervella et al. 2015a,b). At a distance of 64 pc, L_2 Puppis is one of the nearest and brightest AGB stars, orbited by a close binary companion, and thus represents a unique laboratory in which to test models of the late-stages of stellar evolution.

Adaptive optic imaging revealed the presence of a optically thick, circumstellar disk with wide-bipolar outflows (Kervella et al. 2015a). Its M5III spectral type (Dumm & Schild 1998) implies that L_2 Puppis has an approximately 3500 K effective temperature. Photometric study shows that it is an variable star with apparent magnitude varies from 2.60 to 6.00 with a stable period of 140.6 days (Samus et al. 2009; Bedding et al. 2002) representative of a typical period associated with thermal pulsation (Bowen 1988). The derived radius of L_2 Puppis is $123 \pm 14 R_\odot$ (Kervella et al. 2014) thus its luminosity is $2000 \pm 700 L_\odot$. To fit L_2 Puppis

in Hertzsprung-Russell diagram, a ZAMS evolution model computed by Bertelli et al (2008) implies that L_2 Puppis is now a $2^{+1.0}_{-0.5} M_\odot$ and an age of $1.5^{+1.5}_{-1.0} Gyr$ AGB star.

L_2 Puppis has a large lobe structure that extends more than 10 AU to the northeast of the disk in L-band images (Kervella et al. 2014), likely due to the interaction of an AGB wind with the secondary star. A recent result by Kervella et al. (2015a) supports this hypothesis, revealing evidence of a close-in secondary source at a projected separation of 2 AU. In addition, the existence of an optically-thick dusty circumstellar disk hints at the presence of a secondary. If the disk is stable and in approximate Keplerian motion, it must have high specific angular momentum. However, AGB stars are slow rotators (Meibom, Mathieu & Stassun 2009) and the large difference of specific angular momentum implies that there should be some mechanism that can transfer angular momentum to the gas and dust. A companion can transfer angular momentum to the gas and shape the outflows seen in the post-AGB and PN phases (Nordhaus & Blackman 2006; Nordhaus et al. 2007).

We describe the hydrodynamic simulation in detail in Sect. 2 and present the results in Sect. 3. Sect. 4 discusses the model used in RADMC-3D simulation to generate our synthetic observations. Section 5 compares the results of our synthetic observations to the observation data.

* E-mail: zchen25@ur.rochester.edu

† E-mail: nordhaus@astro.rit.edu

‡ E-mail: afrank@pas.rochester.edu

§ E-mail: blackman@pas.rochester.edu

¶ E-mail: balick@uw.edu

2 HYDRODYNAMIC MODEL DESCRIPTION

We perform three-dimensional hydrodynamic adaptive-mesh-refinement (AMR) simulations of a $2 M_{\odot}$ AGB star with a $0.5 M_{\odot}$ secondary at a separation of $4 AU$. The AGB star is represented as a sphere of radius $1 AU$ with a steady mass-loss rate of $\dot{M}_s = 1.65 \times 10^{-7} M_{\odot}/yr$ and wind velocity of $v_s = 39.3 km/s$. After the simulation reaches steady-state, we eject a pulse of dense wind at a rate of $\dot{M}_p = 9.30 \times 10^{-6} M_{\odot}/yr$ that lasts 11.6 years. The speed of the pulsed material is $v_p = 22.2 km/s$ which is above the escape velocity of the AGB star but below the escape velocity of binary system. The properties of such a pulse are consistent with those expected from the ingestion of a planet by the AGB star. Such events are expected to occur on the giant branches if planetary companions are present and initially orbiting within $\sim 10 AU$ of the main-sequence progenitor (Nordhaus et al. 2010; Nordhaus & Spiegel 2013). Radiation from the AGB star is assumed to be isotropic at all radii with the dust and gas fully coupled. Under such conditions, the radiation force can be expressed as $f_{rad} = \rho \kappa_{total} L / cr^2$ where κ_{total} is the mass weighted opacity of gas and dust. Radiation force is proportional to the gravitational force $f_{grav} = GM\rho/r^2$ in optically thin limit. The total force acting on the gas is thus,

$$f = f_{grav} - f_{rad} = \alpha f_{grav} \quad (1)$$

We assume $\alpha = 0.134$ in our model. Note that once the disk forms, radiation may not be isotropic at all outward radii from the AGB star. The formation of an optically thick region, such as a disk, would block photons such that the interior regions would experience a reduced, or no radiation force. Optically thin regions, such as those in the polar direction (and for the majority of our computational domain) would continue to experience the full radiation force. Despite our use of Eq. 1 everywhere, a prominent disk clearly forms. Thus, future work which reduces the radiation force in optically thick regions should result in lowering the physical conditions under which the disk forms.

Assuming the dust and gas are in local thermal equilibrium (LTE) and that the luminosity from the AGB star is constant, the gas temperature goes as $T \sim \sqrt{r}$. At $\sim 120 R_{\odot}$ the surface temperature of the AGB star is $3500 K$ and is approximately $400 K$ at $40 AU$ away. Since our simulation zone is $80 AU \times 80 AU \times 80 AU$ and we want to form a relatively thin disk feature, we use $400 K$ isothermal condition in our simulation.

To carry out our three-dimensional hydrodynamic simulations, we employ *AstroBEAR*. AstroBEAR is a multi-physics, adaptive-mesh-refinement (AMR) code which employs a Riemann solver to solve the fluid equations (Carroll-Nellenback et al. 2013). In our simulation, we use 100^3 computational cells as the base grid and 3 levels of AMR such that the total effective resolution is 800^3 . The equations of motion of fluid in the simulation are

$$\frac{\partial \rho}{\partial t} + \nabla \cdot (\rho \mathbf{v}) = 0 \quad (2)$$

$$\frac{\partial \rho \mathbf{v}}{\partial t} + \nabla \cdot (\rho \mathbf{v} \mathbf{v}) = -\nabla p - \frac{\alpha G M_1 \hat{\mathbf{r}}_1}{r_1^2} - \frac{G M_2 \hat{\mathbf{r}}_2}{r_2^2} \quad (3)$$

$$p = n k_b T, \quad (4)$$

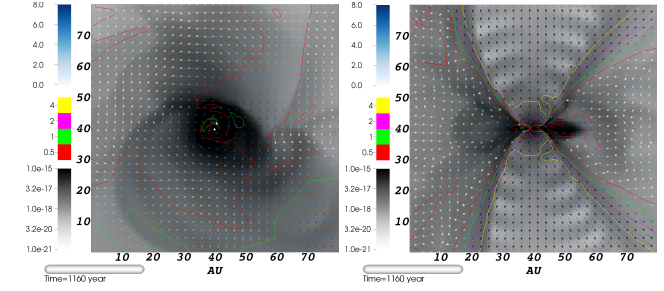


Figure 1. Top: Face-on view of the disk (x-y plane). Bottom: Edge on view of the disk (x-z plane). Density values are shown with a gray-color map, while velocity vectors are shown in white and blue at the end of the simulation. Four contours of q delineate the bound and unbound regions.

where subscript 1 represents the AGB star and subscript 2 represents the secondary. The mean atomic weight of the gas material is $1.3 m_H$.

3 DISK AND OUTFLOW FORMATION

We run the simulation for 1160 years. Approximately, 100 years after the ejection of the dense wind, gas material falls back with a disk forming in the orbital plane. Meanwhile, low-density gas outflows in the polar directions.

To measure whether material is gravitationally bound to the binary system, we devise a parameter,

$$q \equiv \frac{e_k + e_{internal}}{\|\phi\|} = \frac{0.5v^2 + 1.5k_b T}{\|\phi\|} \quad (5)$$

where ϕ is the specific gravitational potential energy of the material. When $q < 1$ the material is bound to the system.

Figure 1 clearly shows the unbound-bipolar outflows and gravitationally-bound disk structure at the end of the simulation. In the top panel, high-density gas is orbiting the binary the locations of which are marked with white triangles. The radius of the disk is roughly $12 AU$ and there is a spiral-arm in the outer disk which sweeps clockwise. The $q = 0.5$ and $q = 1$ iso-contours demonstrate that most of the gas in mid-plane is gravitationally bound though there is some escaping gas in the lower right corner of the top panel. This is to be expected as gas from the mass-losing AGB star continually interacts with the disk. In the right panel, the $q = 4$ iso-contour forms two cones indicating that the gas in the polar direction is not bound. The velocity of the bipolar outflows is roughly $20 km/s$. The disk is clearly seen in Fig. 1 as the dense gravitationally-bound region inside the red iso-contour. In the equatorial region, some of the outflowing gas will fall back onto the the mid-plane and become incorporated into the disk while some will flow out of the system.

4 RADMC-3D MODEL

We employ the RADMC-3D code (Dullemond 2012) to post-process our hydrodynamic results and create synthetic maps for comparison to observations. To do this, we use a Monte Carlo Method (Bjorkman & Wood 2001) with prescribed dust distribution to determine the dust temperature, which

is then used to produce images of photon density under the assumption of isotropic scattering. The results of our hydrodynamic simulation serve as the input for the radiation transfer simulation.

4.1 Spectral Energy Distribution

We adopt an AGB photospheric model from Castelli & Kurucz (2004) which is shown as the blue curve in Figure 3. The AGB model has an effective temperature of $3500K$, $\log g = 1.5$ and $[M/H] = 0.0$. The raw SED is subject to reddening of $E(B-V) = 0.6$ with a standard Milky Way $R_V = A_V/E(B-V) = 3.1$ interstellar dust model and shown as green curve in Figure 3 Fitzpatrick (1999).

4.2 Dust species and spatial distribution

Observational studies of L_2 Puppis show that there is an infrared excess in the SED indicative of dust in the system (Kervella et al. 2014, 2015a). Such infrared excesses in evolved stars are associated with dust shells or disks Nordhaus et al. (2008). Furthermore, the $10\ \mu m$ feature suggests the dust is primarily silicate-based. As such, we choose two kinds of amorphous silicates: $MgFeSiO_4$ olivine and $MgFeSi_2O_3$ pyroxene (Jaeger et al. 1994; Dorschner et al. 2004). The dust is assumed to be spherical with dust size distribution going as $dn \sim a^{-3.5}da$ (Mathis, Rumpl & Nordsieck 1977) for both kinds of dust where a is the dust radius and dn is the number density. The dust radius we consider ranges from $0.1\mu m$ to $0.3\mu m$.

Dust can not form when the environment is too hot. Therefore, the dust-to-gas mass ratio is set to zero within $4AU$ of the center-of-mass of the binary where gas temperatures are typically above dust sublimation temperatures. For the rest of the computational domain, we set $\eta = 0.01$ since small dust grains are almost fully coupled with the fluid (Mastrodemos & Morris 1998). We assume that 80% mass of the dust is olivine and 20% mass of the dust is pyroxene.

In reality, dust grains tend to conglomerate when the temperature drops (Gail et al. 2013) and large-dust grains do not as easily couple to the fluid. Therefore, we may underestimate the dust contribution in dense regions such as the disk itself (Woitke 2006). However, by assuming a fixed dust distribution, composition, and gas-to-dust ratio, the problem is tractable with current computational resources. We leave self-consistent multi-fluid, three-dimensional, radiation-hydrodynamic modeling for future work.

5 RADIATION TRANSFER SIMULATION RESULTS

In Figure 2, we compare the synthetic V-band and N-band RADMC-3D images with the corresponding ZIMPOL observations (Kervella et al. 2015a). Figure 3 shows the broadband SED of our hydrodynamic model and observational data (detail can be found in Kervella et al. (2014, 2015a)). We successfully reproduce the $1\mu m$ to $4\mu m$ flat feature and the $10\mu m$ bump in the SED while matching the V- and N-band images.

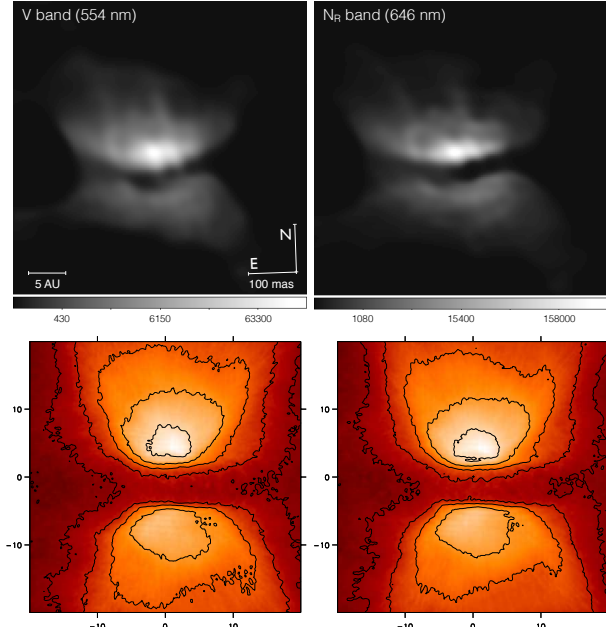


Figure 2. Synthetic V-band and N-band images from our hydrodynamic simulation compared to the corresponding ZIMPOL observations for the same logarithmic scale. The dimension and the inclination of our images are $40\ AU \times 40\ AU$ and 82° respectively.

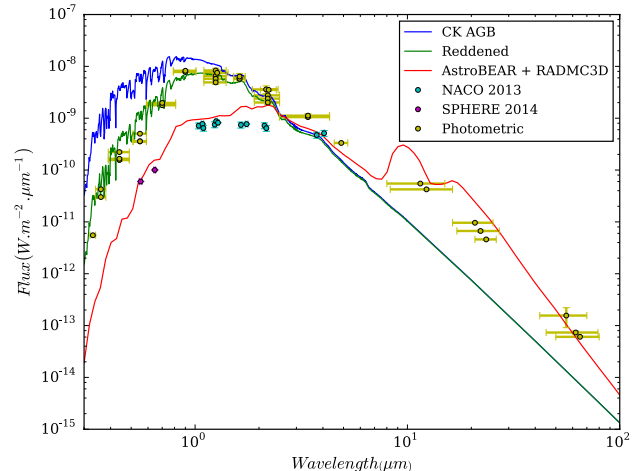


Figure 3. Spectral energy distribution of L_2 Puppis .

Figure 2 clearly shows there is an optically thick circumstellar torus in V and N band.

6 SUMMARY AND DISCUSSION

In this paper, we present a fully 3-D hydrodynamic simulation that incurs a pulse of dense wind followed by constant stellar wind in a binary system. Our simulation self-consistently forms a circumbinary disk with wide-bipolar outflows for the L_2 Puppis system parameters. The approach of hydrodynamic modeling coupled with the comparison of synthetic observations to broad-band photomet-

ric and imaging data significantly improves upon previous non-dynamical, morphological studies of L_2 Puppis .

For our computational domain, we track whether the fluid is gravitationally bound or escaping. The bulk of the bound material is in the circumstellar disk in the orbital plane. In the polar directions, wide-low-velocity outflows emerge with measured velocities of ~ 20 km/s. Synthetic radiative transfer results post-processed from our simulation shows overall morphological similarity to the V-band and N-band SPHERE observations. The broad-band SED matches well, reproducing the “flat” range from $1\mu\text{m}$ to $4\mu\text{m}$ and the infrared excess seen long-ward of $10\mu\text{m}$. This study is an initial step in applying photometric and imaging observations to fully dynamical three-dimensional simulations of evolved binary star systems. Future work should include additional physical effects such as cooling, self-consistent radiative transfer and multi-dust species.

REFERENCES

Balick, B., & Frank, A. 2002, ARA&A, 40, 439

Balick, B. 1987, AJ, 94, 671

Bedding, T. R., Zijlstra, A. A., Jones, A., et al. 2002, MNRAS, 337, 79

Bertelli, G., Girardi, L., Marigo, P., & Nasi, E. 2008, A&A, 484, 815

Bjorkman, J. E., & Wood, K. 2001, ApJ, 554, 615

Bowen, G. H. 1988, ApJ, 329, 299

Carroll-Nellenback J. J., Shroyer B., Frank A., Ding C., 2013, JCoPh, 236, 461

Castelli, F., & Kurucz, R. L. 2004, ArXiv e-prints [arXiv:astro-ph/0405087]

Chen, Z., Frank, A., Blackman, E. G., & Nordhaus, J., 2016, ArXiv e-prints [arXiv:1505.02969]

De Marco, O. 2009, PASP, 121, 316

Dorschner, J., Begemann, B., Henning, T., Jaeger, C., & Mutschke, H. 1995, A&A, 300, 503

Dullemond, C. P. 2012, RADMC-3D: A multi-purpose radiative transfer tool, astrophysics Source Code Library

Dumm, T., & Schild, H. 1998, New A., 3, 137

Fitzpatrick, E. L. 1999, PASP, 111, 63

Gail, H.-P., Wetzel, S., Pucci, A., & Tamanai, A. 2013, A&A, 555, A119

Jaeger, C., Mutschke, H., Begemann, B., Dorschner, J., & Henning, T. 1994, A&A, 292, 641

Kervella, P., Montagès, M., Ridgway, S. T., et al. 2014, A&A, 564, 88

Kervella, P., Montagès, M., Legadec, E., et al. 2015, A&A, 578, 77

Kervella, P., Montagès, M., & Lagadec, E. 2015, EAS Publications Series, 71, 211

Krumholz, M. R., Klein, R. I., McKee, C. F., Offner, S. S. R., & Cunningham, A. J. 2009, Science, 323, 754

Mastrodemos, N. & Morris, M. 1998, ApJ, 497, 303

Mathis, J. S., Rumpl, W., & Nordsieck, K. 1977, ApJ, 217, 425

Meibom, S., Mathieu, R.D., & Stassun, K.G. 2009, ApJ, 695, 679

Nordhaus, J., & Blackman, E. G. 2006, MNRAS, 370, 2004

Nordhaus, J., Blackman, E. G., & Frank, A. 2007, MNRAS, 376, 599

Nordhaus, J., Minchev, I., Sargent, B., et al. 2008, MNRAS, 388, 716

Nordhaus, J., Spiegel, D. S., Ibgui, L., Goodman, J., & Burrows, A. 2010, MNRAS, 408, 631

Nordhaus, J., & Spiegel, D. S. 2013, MNRAS, 432, 500

Samus, N. N., Durlevich, O. V., et al. 2009, VizieR Online Data Catalog, 1, 2025

Soker, N., & Rappaport, S. 2000, ApJ, 538, 241

Woitke, P. 2006, A&A, 452, 537

This paper has been typeset from a TeX/ L^AT_EX file prepared by the author.